

PCNet: A Structure Similarity Enhancement Method for Multispectral and Multimodal Image Registration

Si-Yuan Cao, Hui-Liang Shen, Lun Luo, Shu-Jie Chen, and Chunguang Li

Abstract—**Multispectral and multimodal images processing is important in the community of computer vision and computational photography.** As the acquired multispectral and multimodal data are generally misaligned due to the alternation or movement of the image device, the image registration procedure is necessary. The registration of multispectral or multimodal image is challenging due to the non-linear intensity and gradient variation. To cope with this challenge, we propose the phase congruency network (PCNet), which is able to enhance the structure similarity and alleviate the non-linear intensity and gradient variation. The images can then be aligned using the similarity enhanced features produced by the network. PCNet is constructed under the guidance of the phase congruency prior. The network contains three trainable layers accompany with the modified learnable Gabor kernels according to the phase congruency theory. Thanks to the prior knowledge, PCNet is extremely light weight and can be trained on quite a small amount of multispectral data. PCNet can be viewed to be fully convolutional and hence can take input of arbitrary sizes. Once trained, PCNet is applicable on a variety of multispectral and multimodal data such as RGB/NIR and flash/no-flash images without additional further tuning. Experimental results validate that PCNet outperforms current state-of-the-art registration algorithms, including the deep-learning based ones that have the number of parameters hundreds times compared to PCNet. Thank to the similarity enhancement training, PCNet outperforms the original phase congruency algorithm with two-thirds less feature channels.

Index Terms—Multispectral image, multimodal image, image registration, phase congruency theory, similarity enhancement, gradient descent, image pyramid, optimization.

I. INTRODUCTION

Multispectral and multimodal images, such as RGB and near-infrared (NIR) images [1], flash/no-flash images [2], [3], and images acquired under varying illumination condition [4], generally contain much richer information compared to general single RGB image. They are important data for computer vision and computational photography applications including image segmentation [5], scene category recognition [1], and image denoising/deblurring [6], [7]. Pixel-level alignment

This work was supported by the National Natural Science Foundation of China under Grant 81973751 and Grant 62002323. (*Corresponding author: Hui-Liang Shen.*)

S. Y. Cao, H. L. Shen, L. Luo and C. Li are with the College of Information Science and Electronic Engineering, Zhejiang University, Hangzhou 310027, China (e-mail: karlcao@hotmail.com; luolun@zju.edu.cn; shenhl@zju.edu.cn; cgli@zju.edu.cn).

S. J. Chen is with the School of Computer and Information, Zhejiang Gongshang University, Hangzhou 310018, China (e-mail: chenshujie@zjgsu.edu.cn).

of multispectral/multimodal images captured from different sources is the fundamental requirement for these tasks. Nevertheless, multispectral/multimodal images are prone to be misaligned owing to the alternation or movement of image devices [6], [8]. Therefore, registering multispectral/multimodal images is a primary problem for further computer vision and computational photography tasks.

The most intractable aspect for multispectral/multimodal image registration is the ubiquitous intensity and gradient variation among data from different sources [6], [7], [9]. To cope with the above challenge, various image registration methods have been proposed. The registration methods can be categorized into feature-based ones and intensity-based ones [10]. The feature-based methods align the image through the feature detection, feature description, and the transform estimation procedures. The feature-based methods for multispectral/multimodal images has been proposed to cope with the intensity and gradient variation, such as the multispectral interest points [11], the log-Gabor histogram descriptor (LGHD) [12], and the radiation-variation insensitive feature transform (RIFT) [13], etc. Generally speaking, the feature-based methods are typically more efficient but less accurate compare to the intensity-based ones. The intensity-based methods align the image by finding the best correspondence maximizing (or minimizing) specific similarity measures between two images. Various similarity measures have been developed for multispectral/multimodal data, including mutual information (MI) [14], robust selective normalized cross correlation (RSNCC) [6], and matching by tone mapping (MTM) [15]. These similarity measures are normally of complicated forms, making their optimization problematic and time consuming [16]. On the other hand, another kind of intensity-based methods aims to enhance the structural similarity between images by some transform in advance, and then register the transformed images using common registration measure of simple formulas such as sum of squared differences (SSD), sum of absolute differences (SAD), etc. The common measures can be solved efficiently and effectively using concise optimization method like classical gradient descent.

In this work, we propose the phase congruency network (PCNet) as a similarity enhancement method for multispectral/multimodal image registration. PCNet is a trainable network architecture constructed under the guidance of the phase congruency theory [17]. It detects edge structures by estimating the phase congruency of different scales of frequency components. The magnitude of the output features of our

PCNet merely depends on the congruency of phase among different frequency scales. Therefore, the similarity of output features will be significantly enhanced under the non-linear intensity and gradient variation. It is worth noting that compared to the original phase congruency features, the features produced by our PCNet is of better structural similarity. And hence our PCNet is able to produce more accurate registration results with a third of the features compared to the original phase congruency algorithm. Furthermore, thanks to the prior knowledge of the phase congruency theory, the network can be trained quickly on a small amount of multispectral image data, but works satisfactorily on a markedly wide range of multispectral/multimodal datasets. Compared to other convolutional neural networks (CNN) designed for image registration, our PCNet achieves similar or even better registration performance with a considerably fewer number of parameters.

The multispectral/multimodal image registration procedure using PCNet is performed as follows. First, we build the phase congruency architecture with the guidance of the phase congruency theory, using 3 trainable layers for the trainable feature extraction. Second, we employ the modified learnable Gabor kernels for the multi-scale frequency component extraction, which significantly weaken the difficulty of network training while improving the universality of the network. Third, we present the normalized structural similarity loss for the unsupervised learning of our PCNet. Finally, we present the image registration framework using the image pyramid and gradient descent algorithm.

To summarize, the main contributions of this work are as follows:

- Based on the phase congruency theory, we propose phase congruency network (PCNet), which is trainable and can significantly improve the structural similarity between images having non-linear intensity and gradient variation. The network mainly contains two parts, including the phase congruency architecture and the modified learnable Gabor kernels.
- To cope with the problem that no ground truth exists for the phase congruency feature, we design a normalized structural similarity loss depicting the similarity between the output features of PCNet. The network can then be trained in an unsupervised manner.
- We show that thanks to the prior knowledge of phase congruency, our PCNet works effectively on a markedly wide range of multispectral/multimodal datasets, but only needs to be trained on a small amount of multispectral data. Compared to other CNN designed for registration tasks, our PCNet achieves similar or even better registration performance with a considerably lower number of parameters.

II. RELATED WORK

The registration technique for multispectral/multimodal image can be coarsely categorized into intensity-based method and feature-based methods. We will give a brief review for algorithms belonging to both methods. More detailed survey on the image registration technique is referred to [18]–[20].

For the intensity-based methods, we focus on similarity enhancement algorithms as they are generally more efficient and easy to optimize compared to the conventional complicated multispectral/multimodal measures.

Entropy image (EI) [10] obtains the consistent structure leveraging the Shannon entropy [21], which is defined as

$$H(X) = - \sum_{i=1}^n P(x_i) \log(P(x_i)), \quad (1)$$

where X is a discrete random variable with possible values $\{x_1, \dots, x_n\}$ and probability mass function $P(X)$. For a local area, EI adopts local histogram to compute the probability of different intensity levels, and then computes the entropy as the enhanced structure.

Census transform (CT) [22] encodes the consistent structure by a fixed pattern. The most common version of CT can be expressed as

$$\xi(I(p), I(q)) = \begin{cases} 0 & \text{if } I(p) > I(q) \\ 1 & \text{otherwise} \end{cases}. \quad (2)$$

As CT generally operates on a 3×3 window, a feature of 8 channels for each pixel is obtained as the similarity enhanced structure against the non-linear intensity and gradient variation.

Structure consistency boosting (SCB) transform [16] accomplishes the structural consistency using the statistical prior from the natural image. The consistent inherent edge structures are enhanced leveraging

$$\begin{aligned} \mathcal{S}(p; c, \alpha, \beta) \\ = \frac{1}{N-1} \sum_{q \in \mathcal{N}_p} \frac{\delta^2(p, q)}{\delta^2(p, q) + c \cdot \exp\left(-\left|\frac{\bar{I}(p)-0.5}{\beta}\right|^\alpha\right)}, \end{aligned} \quad (3)$$

where $\delta(p, q)$ indicates the gradient information between image positions p and q . The parameters of SCB are determined using machine learning, which further improves the consistency of the output feature.

Dense adaptive self-correlation (DASC) [23] descriptor is also a similarity enhancement algorithm leveraging machine learning technique. The algorithm is established based on the local self similarity prior. The similarity between patches in a local support window is calculated and then encoded into a descriptor. The optimal sampling pattern for calculating patch similarity is learned using the support vector machine (SVM). An adaptive self-correlation measure is adopted for better depicting the patch-wise similarity.

Several feature-based methods have been proposed for the registration of multispectral/multimodal image. The feature-based methods are typically of more efficiency but less accuracy compared to the intensity-based ones.

Log-Gabor histogram descriptor (LGHD) [12] and radiation-variation insensitive feature transform (RIFT) [13] leverage the log-Gabor filter to alleviate the non-linear variation in intensity and gradient. The LGHD build a histogram for the filter response of each scale of the log-Gabor filter. The combined histogram of different scales finally forms a descriptor. Different from LGHD, RIFT does the summation over each scale of the log-Gabor filter first,

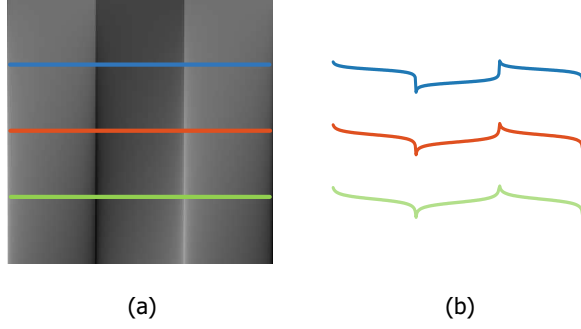


Fig. 1. The constructed grating and its corresponding profiles. (a) the grating constructed using (4). (b) the corresponding profiles from (a).

and then build a maximum index map (MIM) by recording the channel number of the maximum value through different orientations of the log-Gabor filter responses. A histogram similar to SIFT is finally established based on the MIM as the final descriptor.

Recently, many feature-based algorithms based on deep learning frameworks have been proposed. SOSNet [24] adopts the second order similarity regularization for the feature descriptor network training. The second order similarity regularization term enforces a more compact individual cluster for the ground truth matched descriptors, leading to a better matching performance of the feature descriptor. Unlike SOSNet that only learns the feature description stage, SuperPoint [25] and ASLFeat [26] learn the detection and description stage simultaneously. Their network architectures both include a shared encoder, and two separate heads for interest point detection and feature description. To cope with the unlabeled training data, SuperPoint proposes a homographic adaptation process that first trains a weak detector using simulated data, and then trains the network on unlabeled data in a self-supervised manner. ASLFeat introduces deformable convolutional networks (DCN) as part of the network architecture that significantly improves the network performance. A multi-level keypoint detection strategy has also been proposed to boost the detection performance.

III. THE PHASE CONGRUENCY THEORY

In an image, edge features are perceived where different scale of wavelets meets maximum phase congruency [17]. For better illustration, we construct a grating in Fig. 1 (a) using the series

$$\sum_{s=0}^{\infty} \frac{1}{2s+1} \sin((2s+1)x + \phi), \quad (4)$$

where x varies along the horizontal direction, and ϕ the vertical, denoting the congruent phase shift. s denotes the scale of wavelet series. Profiles of different phase shifts are drawn in Fig. 1 (b). We can observe that the congruency of phase at every phase shift produces a clearly perceived feature, namely edge structure of an image.

Practically, the phase congruency feature is computed by first convolving the image with quadrature pair of wavelet

filters at each scale s . The wavelet filters contain the even-symmetric and the odd-symmetric parts. The frequency responses of the wavelet filters at each scale are denoted by $e_s(x, y)$ for the even and $o_s(x, y)$ for the odd. We can then compute the amplitude of response at each scale by

$$A_s(x, y) = \sqrt{e_s(x, y)^2 + o_s(x, y)^2}, \quad (5)$$

and the phase by

$$\phi_s(x, y) = \arctan(o_s(x, y)/e_s(x, y)). \quad (6)$$

The local energy can then be computed by

$$E(x, y) = \sqrt{(\sum_s e_s(x, y))^2 + (\sum_s o_s(x, y))^2}, \quad (7)$$

and its corresponding phase by

$$\bar{\phi}(x, y) = \arctan(\sum_s o_s(x, y) / \sum_s e_s(x, y)). \quad (8)$$

For clarity, we refer to the phase of multi-scale filter response as phase (denoted by $\phi_s(x, y)$), and the phase of local energy as mean phase (denoted by $\bar{\phi}(x, y)$) in the following.

The phase congruency of some point can be measured by the ratio of the local energy and the accumulation over scales of the amplitude of response

$$PC_0(x, y) = \frac{E(x, y)}{\sum_s A_s(x, y) + \xi} = \frac{\sum_s A_s(x, y) \cos(\phi_s(x, y) - \bar{\phi}(x, y))}{\sum_s A_s(x, y) + \xi}, \quad (9)$$

where ξ is a small value that avoids division by zero. It is claimed that the above phase deviation estimation calculation is prone to produce blurry phase congruency edge features [17]. In order to endow the phase deviation estimation with more ocular discriminability, a correction term is added in. The phase congruency of some point is then formulated as

$$PC_1(x, y) = \frac{\sum_s A_s(\cos(\phi_s - \bar{\phi}) - |\sin(\phi_s - \bar{\phi})|)}{\sum_s A_s + \xi}, \quad (10)$$

where the pixel position (x, y) is omitted to simplify notation.

The features extracted by the phase congruency procedure can weaken the inconsistency of the original image edge. For the multispectral or multimodal image, the phase congruency procedure is able to enhance the structure consistency regardless of the non-linear variation in image intensity and gradient. However, the present phase congruency procedure is of quite a lot drawbacks as it is over sensitive to image noise and fake edges. To produce satisfactory similarity enhancement results for multispectral/multimodal image registration, we construct a trainable network called phase congruency network (PCNet) leveraging the phase congruency theory.

IV. PHASE CONGRUENCY NETWORK FOR STRUCTURAL SIMILARITY ENHANCEMENT

Based on the phase congruency theory [17], we propose our phase congruency network (PCNet). Several modification strategies are put forward for the network construction. Fig. 2 depicts the schematic of our PCNet. The input images are first

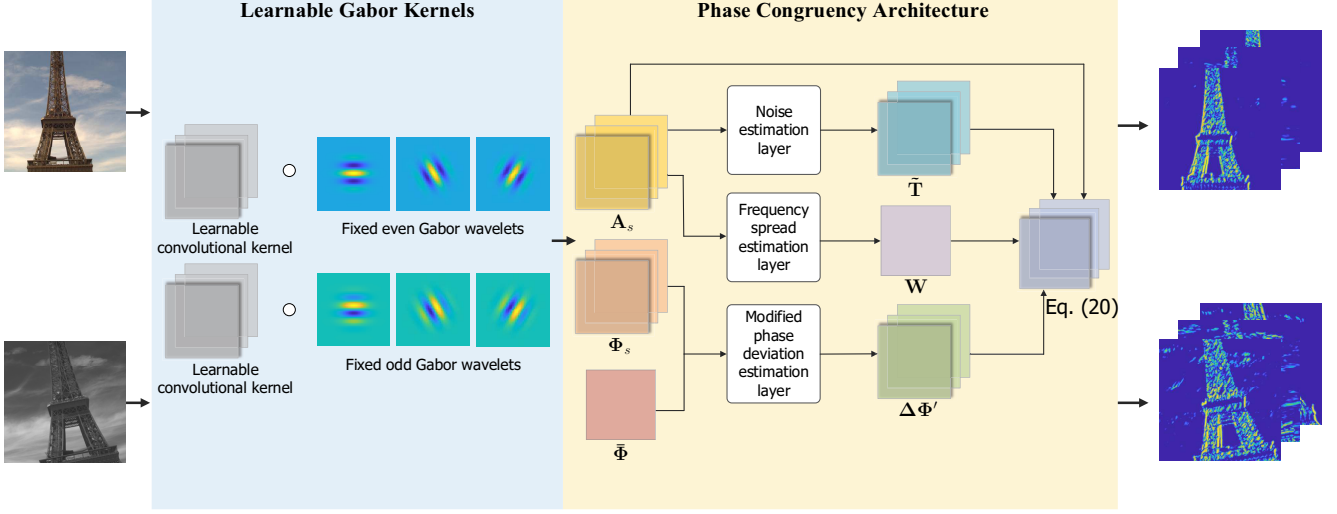


Fig. 2. The schematic of the phase congruency network. The networks are constructed based on the phase congruency theory. 3 trainable layers: noise estimation layer, frequency spread estimation layer, and modified phase deviation estimation layer are combined into the networks. The learnable Gabor kernels are also employed as the quadrature wavelet bank which satisfying the phase congruency theory.

convolved by the learnable Gabor kernels, and then fed into the phase congruency architecture. The similarity enhanced structure outputs are finally produced by PCNet. The learnable Gabor kernels consists of the learnable convolutional kernels and the fixed Gabor wavelets. The Gabor wavelets contain quadrature pair of wavelets, and are steerable and scalable, which perfectly satisfies the phase congruency theory. The phase congruency architecture are constructed based on the aforementioned theory with 3 trainable layers, namely the noise estimation layer, the modified phase deviation estimation layer, and the frequency spread estimation layer. We will describe the detail of our PCNet in the following.

We first reformulate (10) into a more compact form for the tensor manipulations in deep-learning frameworks as follows,

$$\mathbf{P} = \left(\sum_s \mathbf{A}_s \circ \Delta \Phi_s \right) \oslash \left(\sum_s \mathbf{A}_s + \xi \cdot \mathbf{1} \right), \quad (11)$$

where \oslash denotes the pointwise division or Hadamard division [27]. $\mathbf{1} \in \mathbb{R}^{H \times W}$ is an all one matrix. $\xi \cdot \mathbf{1}$ here is to prevent the Hadamard division from dividing zero, which will be omitted in the following. $\mathbf{P} \in \mathbb{R}^{H \times W}$, $\mathbf{A}_s \in \mathbb{R}^{H \times W \times S}$, and $\Delta \Phi_s \in \mathbb{R}^{H \times W \times S}$, with S being the amount of filter scales. $\Delta \Phi_s$ indicates the phase deviation estimation layer, which is defined by

$$\Delta \Phi_s = \cos(\Phi_s - \bar{\Phi}) - |\sin(\Phi_s - \bar{\Phi})|, \quad (12)$$

where Φ_s denotes the phase map of an image, and $\bar{\Phi}$ denotes the mean phase map.

In order to obtain satisfactory similarity enhancement results for image registration task, 3 trainable layers are proposed and then combined into PCNet.

A. Noise Estimation Layer

The computation of phase congruency leveraging (11) is sensitive to noise, as in the natural image noise forms small edges. Therefore, the noise should be estimated and eliminated

before computing the phase congruency. As illustrated previously, the local energy is the square root of two independent random variables each following a standard normal distribution. Thus the noise of the local energy will have a Rayleigh distribution [28]. We denote \mathbf{M}_R as the mean of the Rayleigh distribution, which can be obtained by

$$\mathbf{M}_R = \sqrt{\frac{\pi}{2}} \cdot \mathbf{V}_G. \quad (13)$$

We denote \mathbf{V}_R as the variance of the Rayleigh distribution, which is computed by

$$\mathbf{V}_R = \sqrt{\frac{4 - \pi}{2}} \cdot \mathbf{V}_G. \quad (14)$$

The Rayleigh noise map can then be estimated by the form

$$\mathbf{T} = \mathbf{M}_R + \mathbf{V}_R. \quad (15)$$

\mathbf{V}_G in (13) and (14) indicates the variance of the end position of the local energy vector, which can be estimated by

$$\mathbf{V}_G = \tau \cdot (\mathbf{1} - (1/\alpha)^{\circ N_s}) \oslash (\mathbf{1} - \mathbf{1}/\alpha + \xi \cdot \mathbf{1}), \quad (16)$$

where N_s denotes the number of the frequency scales, and \circ denotes the pointwise power or Hadamard root [29]. τ can be directly estimated from the local energy. Note that the original α here is defined as the scaling factor between successive filters, but in this work we make α a trainable unit as it directly controls the overall noise threshold. Unit α will be updated by the gradient flow in the training stage, thus making the Rayleigh noise map into the noise estimation layer of our PCNet.

Once having the threshold produced by the noise estimation layer, the noise can be removed by a soft thresholding strategy

$$f(m) = \begin{cases} m - t & \text{if } m > t \\ 0 & \text{if } m \leq t \end{cases}, \quad (17)$$

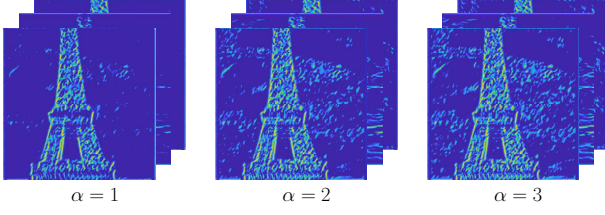


Fig. 3. Phase congruency outputs generated by different α s.

where t denotes the estimated threshold. For our PCNet, the soft thresholding operation can be perfectly modified into the rectified linear units [30], namely the ReLU structure. And then the noise removed PCNet is formulated as

$$\mathbf{P} = \sum_s \text{ReLU}(\mathbf{A}_s \circ \Delta\Phi_s - \tilde{\mathbf{T}}) \oslash \sum_s \mathbf{A}_s, \quad (18)$$

where $\tilde{\mathbf{T}} \in \mathbb{R}^{H \times W \times S}$ indicates the dimension-expanded version of \mathbf{T} having S replicas along the scale dimension.

We illustrate the phase congruency outputs generated by different α s in Fig. 3 for the RGB image in Fig. 2. It is observed that the image noise can be removed more thoroughly as α decreases, at the expense of more edges being eliminated.

B. Modified Phase Deviation Estimation Layer

The original phase deviation estimation layer according to [17] is formed by (12). The added correction term is able to make the output phase congruency features thinner visually. However, it is not clear that ocular discriminability is beneficial to the structure similarity enhancement task. Therefore, we employ a trainable term β into the phase deviation estimation layer, yielding the modified phase deviation estimation layer

$$\Delta\Phi'_s = \cos(\Phi_s - \bar{\Phi}) - \beta \cdot |\sin(\Phi_s - \bar{\Phi})|. \quad (19)$$

We then demonstrate the phase congruency outputs with various β s in Fig. 4. It is observed that the ocular discriminability of the phase congruency features evidently grows as β increases, but the output structures become much weaker in the mean time.

C. Frequency Spread Estimation Layer

As described in the preceding paragraph, the phase congruency aims to measure the consistency of different scales of frequency components. However, (11) is unable to estimate how many scales of frequency are congruent. One extreme case is that the signal only contains one scale of frequency

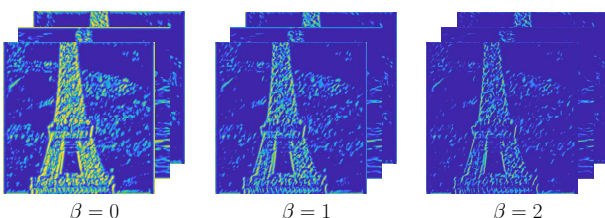


Fig. 4. Phase congruency outputs generated by different β s.

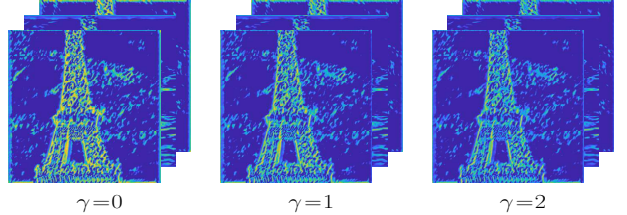


Fig. 5. Phase congruency outputs generated by different γ s.

(e.g. the sine wave) would be considered to have good phase congruency at every position. The phase congruency calculation would detect fake edges under this circumstance. To handle this drawback, frequency spread estimation layer is employed by first calculating the frequency spread map

$$\mathbf{D} = \frac{1}{S-1} \cdot ((\sum_s \mathbf{A}_s) \oslash \max_s(\mathbf{A}_s) - 1), \quad (20)$$

where $\max(\cdot)$ means the maximum operation along the scale dimension. Then the frequency spread estimation layer can be obtained by

$$\mathbf{W} = \text{sigmoid}(\mathbf{D}, \gamma), \quad (21)$$

where $\text{sigmoid}(\cdot, \gamma)$ denotes the sigmoid function [31] that operates pointwisely on the frequency spread map \mathbf{D} . Here γ is made into a trainable unit controlling the slope of the sigmoid function, forming the frequency spread estimation layer. The impact of diverse γ s is displayed in Fig. 5. Along with the growth of γ , edge features having better frequency spread are further recognized and enhanced, whereas a too large γ would overmuch vanish the structure information.

By adopting the above trainable layers, our PCNet is finally modified into

$$\mathbf{P}(\alpha, \beta, \gamma) = \mathbf{W} \circ \sum_s \text{ReLU}(\mathbf{A}_s \circ \Delta\Phi'_s - \tilde{\mathbf{T}}) \oslash \sum_s \mathbf{A}_s, \quad (22)$$

With the assistance of the phase congruency theory, we now construct a network architecture with trainable units. However, we still need a proper set of wavelet filters for the multi-scale frequency component extraction.

D. Modified Learnable Gabor Kernels

It is a straightforward idea to construct a series of convolutional neural networks (CNN) for the multi-scale frequency component extraction. However, there is no ground truth phase congruency feature for the CNN training. Furthermore, the filters at large-scale generally require huge patch size, which further increases the difficulty of the network training.

Considering the these issues, we adopt the learnable Gabor kernels as part of the network architecture for the multi-scale frequency component extraction. The Gabor filters or Gabor wavelets are steerable and scalable filters created by Dennis Gabor [32]. It is claimed that simple cells in the visual cortex of mammalian brains can be modeled by the Gabor functions [33], thus the Gabor wavelets is thought to be similar with the perception of human visual system. What's more, it has been shown that the shallow layers of image trained CNN tend to

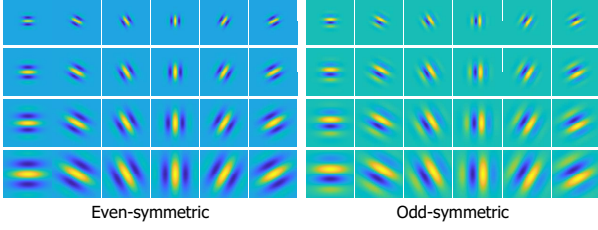


Fig. 6. Examples of the steerable and scalable Gabor wavelets.

learn features resembling Gabor filters [34], [35]. Gabor filters are composed of a pairwise bank of multi-scale quadrature wavelets, which perfectly satisfy the requirement of PCNet. The Gabor wavelets are defined as [36]

$$G_{u,v}(\mathbf{z}) = \frac{\|\mathbf{k}_{u,v}\|^2}{\sigma^2} e^{-\|\mathbf{k}_{u,v}\|^2 \|\mathbf{z}\|^2 / 2\sigma^2} (e^{i\mathbf{k}_{u,v}^\top \mathbf{z}} - e^{-\sigma^2/2}). \quad (23)$$

Examples of Gabor wavelets are displayed in Fig. 6. The even-symmetric part is at left and the odd at right. The orientation of filters varies along the horizontal direction and the scale the vertical.

The Gabor filters are made learnable by the pointwise production with the learnable convolutional kernels having the same patch size [35], as depicted in Fig. 2. The original purpose of introducing Gabor wavelet into the CNN architecture in [35] is to guide the learnable convolutional kernels with directional information, which lighten the deep networks for image classification and improves its performance. On the contrary, in our work, the modulation provides the CNN layer with more constraint, which significantly reduce the difficulty of the network training. It is worth noting that compared to [35], our learnable Gabor kernels are markedly different at 3 aspects:

- We employ the full parts (even-symmetric and odd-symmetric) of Gabor wavelets that satisfy the phase congruency theory, while [35] only uses the even-symmetric part to guide the direction of convolution kernels for the classification purpose.
- We achieve the multi-scale convolution by directly enlarging the size of kernels at different scales that perfectly matches the requirement of phase congruency theory, whereas [35] by resizing the input features using the max pooling operation.
- Considering that the Gabor filters are of the drawback that being over sensitive to the DC component of the signal, we modify the Gabor wavelets by subtracting their corresponding averages.

To better illustrate the effectiveness of our modification, we draw the filter responses together with the phase congruency outputs for the original Gabor filters and the modified ones in Fig. 7. It is observed that without the modification for the Gabor filters, the filter has obvious response for the DC components of the image. As a result, the corresponding phase congruency output also appears to be sensitive to the DC component. On the contrary, our modified Gabor filters significantly alleviates the above problem.

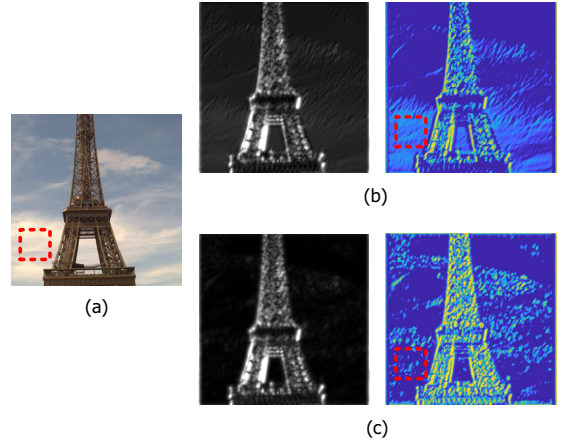


Fig. 7. The filter responses together with the phase congruency outputs for (b) the original Gabor filters and (c) the modified Gabor filters. The red boxes highlight the area for detailed comparison.

For each orientation of the learnable Gabor kernels, our PCNet adopts the corresponding filter outputs and produces one channel of the phase congruency map. At last, channels of map form multi-channel phase congruency features for the whole image. The dimension of the features is determined by the orientation number of the learnable Gabor kernels. By denoting o as the orientation, the calculation of our PCNet is finally formulated as

$$\mathbf{P}_o(\alpha, \beta, \gamma) = \mathbf{W}_o \circ \sum_s \text{ReLU}(\mathbf{A}_{s,o} \circ \Delta \Phi'_{s,o} - \tilde{\mathbf{T}}_o) \otimes \sum_s \mathbf{A}_{s,o}. \quad (24)$$

E. Normalized Structural Similarity Loss for Unsupervised Network Training

The PCNet can be trained by the stochastic gradient descent (SGD) [37] algorithm accompanied with a proper loss function. However, as mentioned in the previous subsection, no ground truth phase congruency feature exists for the training process. We decide to employ a loss function that directly compares the pairwise similarity of the output phase congruency features of two input multispectral or multimodal images. In this way, an unsupervised learning framework is established, which perfectly matches our requirement of enhancing structural similarity of the input images.

The network is trained in a siamese strategy. Let I_1 and I_2 be two original band images, and \mathbf{P}_1 and \mathbf{P}_2 be the outputs after applying our PCNet. Considering that the phase congruency features of our PCNet is more like the edge structure of the image, we first employ SSIM for measuring the similarity of \mathbf{P}_1 and \mathbf{P}_2 , which can be denoted by

$$S = \sum_o \text{SSIM}(\mathbf{P}_1, \mathbf{P}_2) / N_o, \quad (25)$$

where o denotes the orientation of the learnable Gabor kernels, ranging from 1 to N_o . Note that the loss function is generally

minimized by the back propagation algorithm, we can then obtain the loss function

$$L = 1 - \sum_o \text{SSIM}(\mathbf{P}_{1,o}, \mathbf{P}_{2,o})/N_o. \quad (26)$$

Here comes a problem that the above loss function tends to produce an ambiguous guide for the network training. For example, a pair of outputs with all 0 intensity will produce a minimized loss function with the value being 0. The structural content of the image will be exterminated and the following registration procedure will fail. To cope with this, we adopt the gradient of an image to protect its structural information, yielding the modified loss function

$$L = \frac{1 - \sum_o \text{SSIM}(\mathbf{P}_{1,o}, \mathbf{P}_{2,o})/N_o}{|\sum_l \sum_o (\|\nabla_l \mathbf{P}_{1,o}\|_1 + \|\nabla_l \mathbf{P}_{2,o}\|_1)/N_o|^c}, \quad (27)$$

where the operator ∇_l , with $l \in \{x, y\}$, represents the gradient operator along the horizontal and vertical directions. c is the structure protection parameter that balances the degree of similarity enhancement and structure protection. The networks can then be trained with the SGD algorithm using the above loss function.

F. Hierarchical Motion Estimation Based Image Registration

In this work, we adopt the intensity-based registration algorithm for the registration procedure. The intensity-based method registers the misaligned images by minimizing (or maximizing) similarity measures with reference to the parametric or non-parametric transform. We leverage the sum of squared differences (SSD) as the registration measure. SSD is an effective measure with a very concise form, and its optimization is simple yet robust. SSD has been widely used for a variety of image registration tasks [18]. The registration procedure using SSD can be formulated by

$$\hat{\mathbf{a}} = \underset{\mathbf{a}}{\operatorname{argmin}} \sum_{p \in \Omega(\mathbf{a})} (I_F(p, \mathbf{a}) - I_R(p))^2, \quad (28)$$

where \mathbf{a} denotes the registration parameters for correcting the inconsistency of the coordinate between the reference image I_R and the floating image I_F , $\Omega(\mathbf{a})$ denotes the meaningful overlapping area of the warped I_F . We focus on the affine transform for modeling the registration parameters in this work. The affine transform can handle image deformation such as rotation, scaling, translation, shearing and any combinations of them [38]. As a parametric transform, it has been widely adopted for multispectral and multimodal image registration [7], [39], [40]. The process that the affine transform acts on the image coordinate can be denoted as

$$\begin{pmatrix} u \\ v \end{pmatrix} = \begin{pmatrix} x & y & 1 & 0 & 0 & 0 \\ 0 & 0 & 0 & x & y & 1 \end{pmatrix} \mathbf{a}, \quad (29)$$

where $\mathbf{a} = (a_1, a_2, a_3, a_4, a_5, a_6)^\top$ is the affine transform parameter to be computed, and u, v the warped coordinate. The affine parameters are optimized iteratively using the gradient descent algorithm. The initial registration parameter \mathbf{a}_0 is set to the identical transform, i.e., $\mathbf{a}_0 = (1, 0, 0, 0, 1, 0)^\top$.

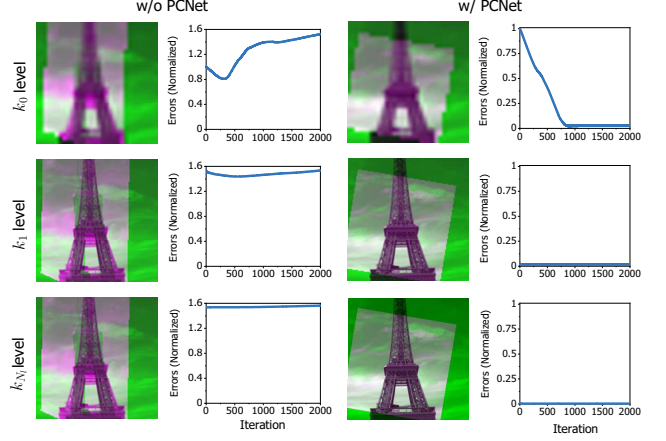


Fig. 8. Hierarchical registration results and registration error plots under the condition of without and with PCNet.

We employ the Gaussian image pyramid for the hierarchical motion parameter estimation [18]. In this work, the coarsest scale of the image pyramid is denoted by k_0 , and the finest by k_{N_l} , with N_l being the total pyramid level number. The registration parameters are updated by the gradient descent optimization, and transferred from the k_0 level to the k_{N_l} . We illustrate the registration result together with the registration error plot for each pyramid level under the condition of without and with our PCNet in Fig. 8. We can find that our PCNet observably improves the registration performance.

V. EXPERIMENTS

PCNet is trained on a small subset of CAVE [8] multispectral dataset, and then evaluated on various multispectral/multimodal datasets, including CAVE and Harvard [41] multispectral band image datasets, RGB/NIR [11] pairwise multispectral image dataset, flash/no-flash [2] and HPatches [4] multimodal datasets. The training subset for our PCNet is not included for the performance evaluation for further fair comparison.

The registration performance of our PCNet is compared with other state-of-the-art similarity enhancement algorithms including the entropy image (EI) [10], census transform (CT) [22], structure consistency boosting (SCB) [16] transform, dense adaptive self-correlation (DASC) descriptor [23]. The original phase congruency algorithm [17] is also included for comparison. The same aforementioned hierarchical registration strategy is employed for all the similarity enhancement algorithms except for DASC. As DASC produce 128-channel output similarity enhancement features, registering the output features directly is too time consuming. Therefore, the registration strategy provided by its public source code¹ is employed, which registers the features point-wisely using SIFT flow [42]. The output flow is then fed into the RANSAC [43] algorithm, producing the affine registration result for fair comparison. We also compare our registration framework using PCNet with the state-of-the-art feature-based methods including log-Gabor

¹<https://seungryong.github.io/DASC/>

histogram descriptor (LGHD) [12], radiation-variation insensitive feature transform (RIFT) [13], SOSNet [24], SuperPoint [25], and ASLFeat [26]. We note that the last 3 methods are based on deep learning frameworks with convolutional neural networks (CNN) being their elementary structures. Considering that the deep learning methods are not trained on multispectral data, we conduct their comparison only on flash/no-flash and HPatches datasets. For all the feature-based methods, the output features are matched using the exhaustive algorithm and the final registration parameters are produced by RANSAC.

We define the registration error as the average Euclidean distance [16] between the pixel positions computed by the ground truth transform \mathbf{a}_{gt} and the estimated transform $\hat{\mathbf{a}}$,

$$e = \frac{1}{M} \sum_p \|\tilde{p}(p, \mathbf{a}_{gt}) - \tilde{p}(p, \hat{\mathbf{a}})\|_2, \quad (30)$$

where M indicates the number of pixels of an image, and \tilde{p} the warped pixel position by applying the transform \mathbf{a} on pixel p . For each dataset, several statistics of the registration errors are computed for more detailed illustration of the registration performance. The statistics includes the mean, median, trim-mean, and the mean of the errors below 25th, 50th, 75th, and 95th percentiles (denoted by best25%, best50%, best75% and best95%). In this way, the error distribution can be depicted comprehensively and concisely.

In order to extensively evaluate the registration performance of each algorithm, we keep the reference image fixed and warp the floating image with simulated transform of three degrees, including the small deformation $\mathbf{a}_{gt,s} = (1.1, 0.1, -10, -0.1, 1.1, 10)^T$, middle deformation $\mathbf{a}_{gt,m} = (1.15, 0.15, -15, -0.15, 1.15, 15)^T$, and large deformation $\mathbf{a}_{gt,l} = (1.2, 0.2, -20, -0.2, 1.2, 20)^T$. In the following experiments, all degrees of simulated transform are adopted if not specially mentioned.

In the following, we first discuss some issues of our PCNet, including the training details and the hyper parameter setting. We then compare our PCNet with the aforementioned registration algorithms. The advantage of our PCNet over the original phase congruency algorithm is also explored in advance. We then analyze the number of parameters of our PCNet and other CNNs designed for the registration task. Finally we conduct the ablation study of our PCNet.

A. Training Details and Hyper Parameter Setting

Our PCNet is trained by a subset of the CAVE [8] dataset. The dataset consists of 32 multispectral image scenes, each including 31 band images ranging from 400 nm to 700 nm. Example images for the CAVE dataset are displayed in Fig. 9(a). The first 10 scenes in alphabetical order are taken as the training data and the rest as test data. Specifically, we randomly crop 20000 pairs of patch with the size of 150×150 for the training stage. The patches are fed into the training process with data augmentation in the brightness, contrast, saturation, and affine deformation. Note that our PCNet can be viewed to be fully convolutional, which means that the



Fig. 9. Example multispectral images in the visible spectrum (displayed in RGB) from the (a) CAVE and (b) Harvard datasets. The scenes to be used for illustration are marked with *SI*.

TABLE I
ERROR STATISTICS OF PCNET UNDER VARIOUS HYPER PARAMETER c ON CAVE DATASET. THE BEST ONES ARE IN BOLD.

c	Mean	Med.	Tri.	Best 25%	Best 50%	Best 75%	Best 95%
0.6	7.94	0.21	0.31	0.05	0.09	0.19	4.84
0.7	6.09	0.20	0.26	0.04	0.08	0.17	3.77
0.8	6.23	0.21	0.28	0.04	0.09	0.18	3.96

TABLE II
ERROR STATISTICS OF PCNET UNDER VARIOUS HYPER PARAMETER N_o ON CAVE DATASET. THE BEST ONES ARE IN BOLD.

N_o	Mean	Med.	Tri.	Best 25%	Best 50%	Best 75%	Best 95%
3	7.42	0.20	0.27	0.04	0.09	0.17	4.35
6	6.09	0.20	0.26	0.04	0.08	0.17	3.77
9	6.05	0.20	0.26	0.04	0.08	0.17	3.63

network is able to work on any size of input image regardless of the patch size for the network training.

We then evaluate two hyper parameters that impact the registration performance, which is the structure protection parameter c in (27) and the orientation number of the learnable Gabor kernels N_o in (24). We evaluate the effect of both parameters in terms of the registration accuracy. For the test data of CAVE, we take the 16th band image (i.e. 550 nm) in each scene as the reference image, and generate floating images by imposing the aforementioned simulated transform to all band images. In this manner, we get 2046 image pairs (22 scenes \times 31 bands \times 3 deformation) for registration experiments.

As elaborated previously, hyper parameter c controls the degree of protection for the structural information. Larger c means better protection for the output structure of PCNet. Nevertheless, if c grows too large, the similarity of the output phase congruency features will be violated. Table I lists the error statistics of our PCNet under various hyper parameter c . We can observe that the error statistic supports the above

TABLE III

ERROR STATISTICS PRODUCED BY IMAGE REGISTRATION USING OUR PCNET AND THE CONVENTIONAL PHASE CONGRUENCY ALGORITHMS WITH VARIOUS OUTPUT FEATURE CHANNELS ON THE CAVE DATASET.

Channel	PCNet							PC-org						
	Mean	Med.	Tri.	Best 25%	Best 50%	Best 75%	Best 95%	Mean	Med.	Tri.	Best 25%	Best 50%	Best 75%	Best 95%
6	6.09	0.20	0.26	0.04	0.08	0.17	3.77	8.34	0.23	0.41	0.04	0.09	0.22	5.50
3	7.42	0.20	0.27	0.04	0.09	0.17	4.35	10.75	0.28	5.01	0.04	0.10	1.37	7.76
2	7.32	0.21	0.28	0.04	0.09	0.18	4.33	11.99	0.35	5.28	0.04	0.12	2.40	9.02
1	8.55	0.24	0.40	0.05	0.10	0.22	5.72	12.27	0.36	5.30	0.04	0.12	2.77	9.29

principle. The best registration performance is obtained at $c = 0.7$.

The hyper parameter N_o controls the total orientation number of the learnable Gabor kernels, and thus decides the channel number of output feature of PCNet. Smaller N_o can reduce the channel of output feature, improving the efficiency of the following registration algorithm, with side effect of worse accuracy. On the contrary, larger N_o is likely to produce better registration performance, but the registration efficiency will be sacrificed. Table II lists the error statistics of our PCNet under various hyper parameter N_o . It is observed that the best registration performance can be achieved at $N_o = 9$. However, the improvement of the registration accuracy by increasing the channel number to 9 is almost indistinctive. Therefore, we set the channel number as $N_o = 6$.

We set the scales for the phase congruency estimation as 4, with the scaling factor between successive filters being 2. For different scales of the learnable Gabor kernels, the size of learnable convolutional kernels are set as 7×7 , 13×13 , 19×19 , and 25×25 . It is worth noting that although the above kernels seem to be overly large for the common CNN, they actually function well during our experiments under the regularization of the Gabor wavelets. As for the three trainable layers, we set the initial value of $\alpha = 2$ as it is originally defined as the scaling factor, and we set $\beta = 1$, $\gamma = 1$.

B. Comparison with the Conventional Phase Congruency Algorithm

Thanks to the modification strategy, our PCNet is able to achieve better registration performance than the conventional phase congruency algorithm. We conduct similar registration experiments on the CAVE dataset as in Section V-A. In order to conduct an exhaustive comparison for both algorithms, we explore their registration performance with the output feature having various channels. We note that, the fewer feature channel signifies the higher registration efficiency.

We list the error statistics for both algorithms of feature channels 1, 2, 3, and 6 in Table III. The conventional phase congruency algorithm is denoted as PC-org. We can observe that for all corresponding feature channel, our PCNet produces considerably better results than the original phase congruency algorithm. Furthermore, our PCNet with 2 channels could achieve better registration accuracy than the PC-org with 6 channels, which means 2 \times increase in computation efficiency.

Note that even PCNet of 1 single channel performs comparably with the PC-org of 6 channels.

For the later experiments, we take our PCNet of both 2 channels (denoted as PCNet-2) and 6 (denoted as PCNet-6) channels for a detailed comparison. The conventional phase congruency algorithm with 6 (denoted as PC-org-6) channels will also be included in the following experiments.

C. Results on Multispectral Band Images

In this section, we evaluate our PCNet with other registration algorithms including EI [10], CT [22], SCB [16], DASC [23], LGHD [12], RIFT [13], and PC-org-6 [17] on the CAVE and Harvard datasets. The Harvard dataset contains 77 multispectral images of real world scenes, each with 31 spectral bands ranging from 420 nm to 720 nm. The sample images are displayed in Fig. 9 (b). The scenes employed for further illustration are marked by $S1$. Similar to the experiment setting for the CAVE dataset, we again take the 16th band image (i.e., 570 nm) of each Harvard scene as the reference image, and generate floating images by imposing the simulated transforms $\mathbf{a}_{gt,s}$, $\mathbf{a}_{gt,m}$, and $\mathbf{a}_{gt,l}$. In this way, we totally conduct 2046 image pairs (22 scenes \times 31 bands \times 3 deformations) for image registration experiments on the CAVE dataset and 7176 image pairs (77 scenes \times 31 bands \times 3 deformations) on the Harvard dataset.

We list the error statistics generated by our PCNet together with other registration methods in Table IV. It is observed that PCNet-2 and PCNet-6 achieves the lowest two indicators for almost all the statistics. CT produces the lowest best25% on both dataset, and SCB yields the lowest best50% on Harvard dataset, but their best75% and best95% indicators degenerate a lot compared to our PCNet. For the feature-based methods including LGHD and RIFT, they generates registration results of low accuracy. It is worth noting that PCNet-2 performs nearly comparably with PCNet-6, and they both outperform PC-org-6.

We further demonstrate the structure enhanced outputs for all the similarity enhancement methods together with their corresponding SSD plots in Fig. 10. The maximum of each SSD distribution is normalized to 1. The displayed image are scene $S1$ from Harvard dataset, with the reference image being the band image at 460 nm and the floating at 720 nm. As we can see, the similarity enhancement ability of our PCNet-6 significantly outperforms the EI, SCB, and PC-org-6 at the position of the bag in the reference image. The structure

TABLE IV
ERROR STATISTICS PRODUCED BY IMAGE REGISTRATION USING OUR PCNET TRANSFORM AND OTHER REGISTRATION ALGORITHMS ON THE CAVE AND HARVARD DATASETS. THE BEST ONES ARE IN BOLD.

	CAVE							Harvard						
	Mean	Med.	Tri.	Best 25%	Best 50%	Best 75%	Best 95%	Mean	Med.	Tri.	Best 25%	Best 50%	Best 75%	Best 95%
EI [10]	19.45	1.72	9.40	0.10	0.29	5.90	15.32	18.94	0.30	6.85	0.05	0.10	3.95	12.29
CT [22]	12.25	0.40	6.74	0.03	0.11	3.06	9.76	12.57	0.15	6.71	0.02	0.05	3.47	10.34
SCB [16]	7.82	0.31	2.69	0.04	0.11	0.71	5.46	6.65	0.11	0.22	0.03	0.05	0.11	3.69
DASC [23]	7.60	1.25	1.53	0.50	0.74	1.10	6.00	10.75	1.51	7.65	0.54	0.83	2.76	9.28
LGHD [12]	20.59	3.17	6.78	0.49	1.06	4.03	12.39	18.08	2.69	6.19	0.45	0.91	3.75	10.54
RIFT [13]	13.90	2.65	4.44	0.56	1.03	2.82	7.92	14.32	1.89	3.30	0.46	0.81	1.99	6.07
PC-org-6 [17]	8.34	0.23	0.41	0.04	0.09	0.22	5.50	3.71	0.09	0.10	0.03	0.05	0.07	1.72
PCNet-2 (ours)	7.32	0.21	0.28	0.04	0.09	0.18	4.33	3.07	0.09	0.11	0.04	0.05	0.08	1.22
PCNet-6 (ours)	6.09	0.20	0.26	0.04	0.08	0.17	3.77	2.76	0.08	0.10	0.03	0.05	0.07	0.94

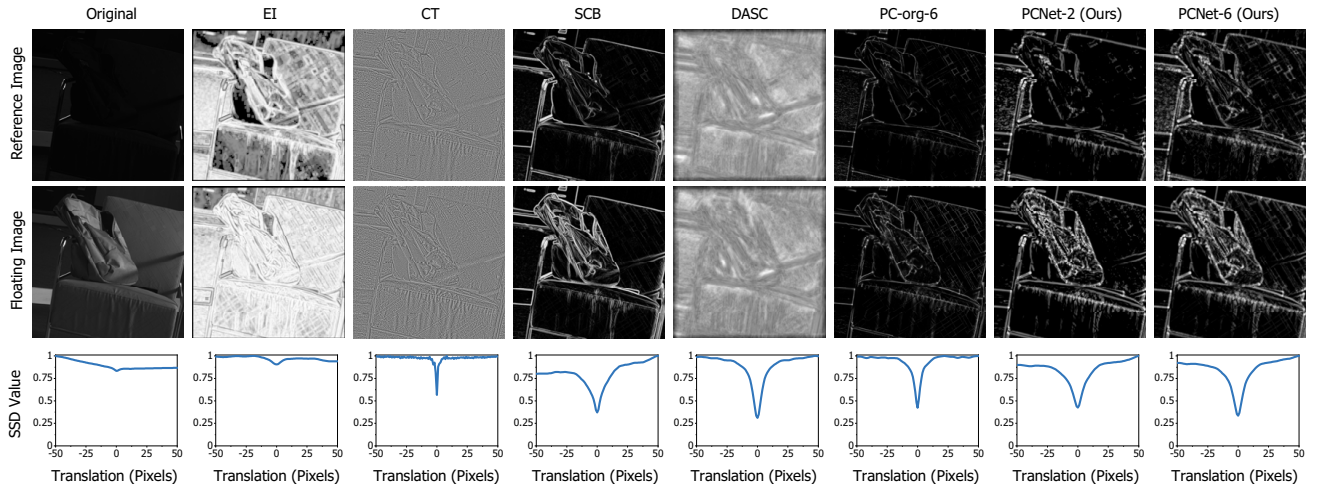


Fig. 10. Comparison of our PCNet and other similarity enhancement algorithms on scene *S1*. First row: the original and transformed reference images. Second row: the original and transformed floating images. Third row: the SSD distributions with respect to the horizontal translation from -50 to 50 pixels.

of our PCNet is markedly conspicuous than the PC-org-6 as our PCNet is trained for similarity enhancement purpose. The outputs of EI show obviously inconsistency with block artifacts and the outputs of CT are excessively noisy. As for the SSD plots, EI gives weak guidance for the best registration position. The SSD plots of CT is too noisy in accordance with the outputs of CT, which may mislead the optimization algorithm. Furthermore, the capture range of the SSD plot of CT is too narrow, which will prevent the optimization algorithm from finding the best match. The SSD plot of SCB fails to indicate the best registration position. In comparison, PCNet-2 and DASC produce SSD plots with larger capture range and stronger minimum peak than any other similarity enhancement algorithms. It is also worth noting that the SSD distributions of PCNet-2 and PCNet-6 are of evidently larger capture range than the PC-org-6 thanks to our similarity enhancement training.

D. Results on RGB/NIR and Flash/no-flash Images

Although PCNet is trained on a relative small dataset of multispectral band image, we show that it can be applied to

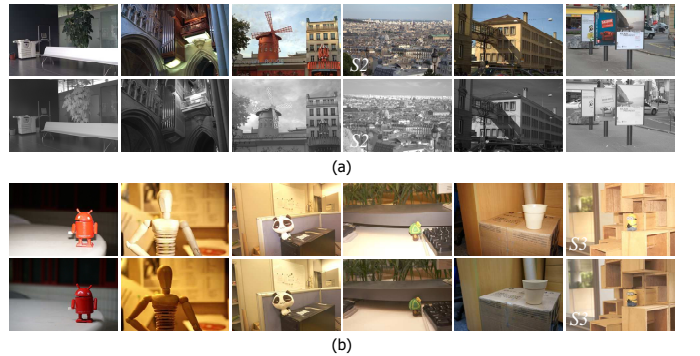


Fig. 11. Example images for RGB/NIR and flash/no-flash datasets. (a) RGB/NIR dataset (b) flash/no-flash dataset. The scenes employed for illustration are marked with *S2* and *S3*.

other multispectral or multimodal datasets without any parameter tuning. We further evaluate our PCNet together with other registration methods on RGB/NIR and flash/no-flash datasets. The RGB/NIR dataset [1] contains 256 RGB/NIR image pairs of various categories of scenes and the flash/no-flash dataset

TABLE V

ERROR STATISTICS PRODUCED BY IMAGE REGISTRATION USING OUR PCNET TRANSFORM AND OTHER REGISTRATION ALGORITHMS ON THE RGB/NIR AND FLASH/NO-FLASH DATASETS. THE BEST ONES ARE IN BOLD.

	RGB/NIR							Flash/no-flash						
	Mean	Med.	Tri.	Best 25%	Best 50%	Best 75%	Best 95%	Mean	Med.	Tri.	Best 25%	Best 50%	Best 75%	Best 95%
EI [10]	19.21	0.42	8.15	0.11	0.18	5.86	13.65	14.36	0.74	6.11	0.20	0.35	2.37	9.68
CT [22]	17.84	11.46	14.05	0.07	0.65	8.24	15.25	12.79	0.60	6.76	0.17	0.29	2.82	10.07
SCB [16]	11.88	0.25	4.57	0.08	0.13	0.97	7.67	5.72	0.43	0.51	0.16	0.24	0.38	3.27
DASC [23]	15.05	2.39	9.44	0.66	1.08	7.32	13.41	9.60	1.54	5.57	0.63	0.91	1.64	8.06
LGHD [12]	15.55	3.92	5.49	0.54	1.21	3.36	8.05	10.11	1.56	2.67	0.50	0.79	1.66	5.07
RIFT [13]	15.21	4.03	5.39	0.61	1.32	3.39	8.17	11.95	1.99	2.96	0.59	0.96	1.91	4.45
PC-org-6 [17]	7.41	0.18	0.23	0.07	0.11	0.16	4.53	4.28	0.40	0.47	0.15	0.23	0.35	2.10
PCNet-2 (ours)	6.09	0.19	0.22	0.08	0.11	0.16	3.53	4.56	0.40	0.46	0.15	0.24	0.35	1.97
PCNet-6 (ours)	6.42	0.18	0.19	0.07	0.10	0.15	3.05	3.42	0.39	0.44	0.15	0.23	0.34	1.40

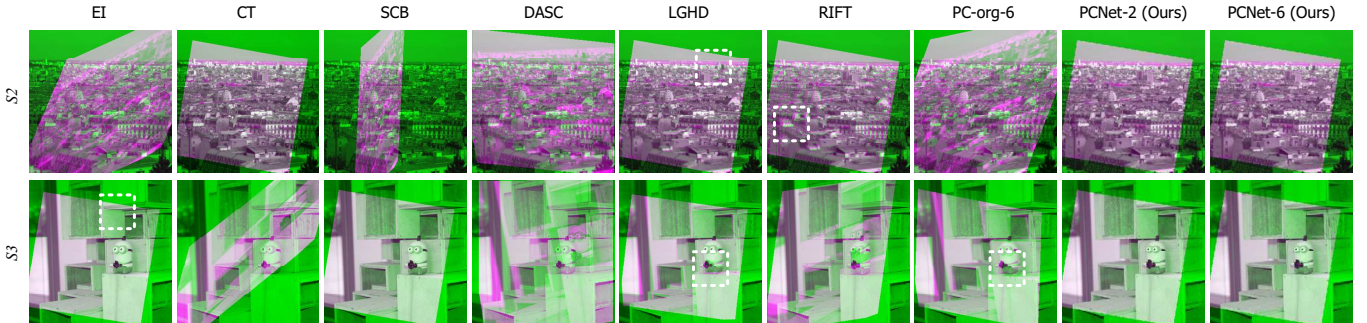


Fig. 12. Registration results produced by PCNet and other registration algorithms, under large degree of transform. First row: registration results of RGN/NIR image pair on scenes S_2 . Second row: registration results of flash/no-flash image pairs on scene S_3 . The white boxes highlight the details for comparison.



Fig. 13. Example images for HPatches dataset.

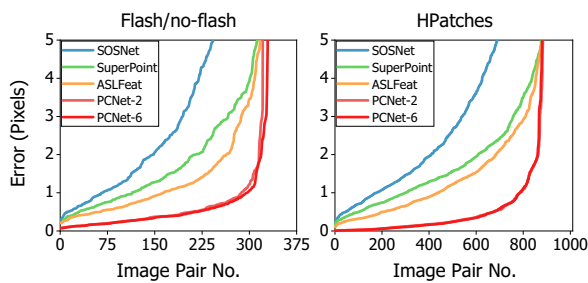


Fig. 14. Registration errors produced by PCNet and other deep learning registration algorithms on flash/no-flash and HPatches datasets. The errors are plotted in ascending order for better illustration.

[2] includes 120 image pairs taken both indoor and outdoor. The example images for both datasets are displayed in Fig. 11. For the RGB/NIR dataset, we set the RGB image as the

reference image and NIR the floating one. For flash/no-flash dataset, we set the flash image as the reference image and no-flash the floating one. The deformation imposed on the floating image are the same as previous experiments. In all, we conduct 768 experiments (256 scenes \times 3 deformations) on the RGB/NIR dataset and 360 experiments (120 scenes \times 3 deformations) on the flash/no-flash dataset.

Table V lists the error statistics of our PCNet together with other registration algorithms. It is observed that our PCNet-2 and PCNet-6 achieves all the lowest indicators on both datasets. The best75% and best95% indicators of PCNet-2 and PCNet-6 are several times smaller than EI, CT, DASC, LGHD and RIFT. What's more, our PCNet-2 keeps better registration accuracy compared to PC-org-6.

Fig. 12 displays the registration results of scene S_2 and S_3 produced by PCNet and other registration algorithms. The registration results are illustrated by overlapping the reference image and the registered floating image and then display them in false color. The white dotted boxes shows the details for comparison. It is observed that for both scenes, only PCNet produces registration result stably and accurately. It is worth noting that for DASC, LGHD and RIFT, they generally produce broadly right registration results yet are lack of precision.

TABLE VI

ERROR STATISTICS PRODUCED BY IMAGE REGISTRATION USING PCNET AND OTHER DEEP LEARNING REGISTRATION ALGORITHMS ON THE FLASH/NO-FLASH AND HPATCHES DATASETS. THE BEST ONES ARE IN BOLD.

	Flash/no-flash							HPatches						
	Mean	Med.	Tri.	Best 25%	Best 50%	Best 75%	Best 95%	Mean	Med.	Tri.	Best 25%	Best 50%	Best 75%	Best 95%
SOSNet [24]	26.95	2.59	3.50	0.79	1.32	2.37	14.95	20.97	2.70	3.33	0.80	1.34	2.30	9.38
SuperPoint [25]	3.26	1.53	1.76	0.58	0.87	1.33	2.06	6.98	1.58	1.76	0.57	0.89	1.30	2.16
ASLFeat [26]	6.58	1.10	1.23	0.44	0.64	0.92	1.79	5.05	1.23	1.39	0.36	0.61	1.00	1.85
PCNet-2 (Ours)	4.56	0.40	0.46	0.15	0.24	0.35	1.97	4.88	0.25	0.34	0.04	0.10	0.22	2.24
PCNet-6 (Ours)	3.42	0.39	0.44	0.15	0.23	0.34	1.40	6.15	0.24	0.34	0.04	0.09	0.21	2.30

TABLE VII

NUMBER OF PARAMETERS OF PCNET AND OTHER DEEP LEARNING BASED REGISTRATION ALGORITHMS.

	SOSNet [24]	SuperPoint [25]	ASLFeat [26]	PCNet-2 (Ours)	PCNet-6 (Ours)
# Parameters	1.3×10^6	1.3×10^6	8.3×10^5	2.4×10^3	7.2×10^3

E. Comparison with Common Deep Learning Methods

It is quite challenging to compare our PCNet with other registration algorithms based on deep learning framework. In this section, we compare our PCNet-2 and PCNet-6 with 3 state-of-the-art registration algorithms using deep CNN, including SOSNet [24], SuperPoint [25], and ASLFeat [26]. As aforementioned, the above networks are not trained on multispectral data, thus we evaluate them on flash/no-flash [2] and HPatches [4] multimodal datasets for fair comparison. For the HPatches dataset, the scenes with photometric changes are taken for evaluation. The first image in each scenes are set as the reference image and all the 6 images of each scene are set as the floating ones. In all, we conduct 1008 (56 scenes \times 6 images \times 3 scenes) registration experiments on HPatches dataset and 360 experiments (120 scenes \times 3 deformations) on the flash/no-flash dataset for each algorithm. The example images for HPatches dataset are displayed in Fig. 13.

We list the error statistics of PCNet and the above mentioned deep learning registration algorithms in Table VI. It is observed that the registration framework using our PCNet is comparable and even better than the state-of-the-art deep learning registration algorithms. Our PCNet is able to produce times lower best25%, best50%, and best75% on both datasets. As for other indicators, our PCNet is also very competitive. This verifies our registration framework are of much better accuracy. We further plot the errors of each registration algorithm in ascending order in Fig. 14. It is observed that compared to the feature-based deep learning registration algorithms, the error of our PCNet is generally lower.

It is worth taking comparison of the number of parameters for the above mentioned deep learning based methods and our PCNet. We list the number of parameters of the above mentioned CNNs and PCNet-2, PCNet-6 in Table VII. It is observed that the number of parameters of our PCNet are two orders of magnitude fewer than common deep learning based algorithms. Moreover, the number of parameters of PCNet-2 is about 500 \times smaller compared to SOSNet and SuperPoint. In all, our PCNet achieves more accurate registration results

with extremely lower computation power requirement.

F. Ablation Study

Finally, we have an ablation study of our PCNet for the noise estimation layer (layer1), modified phase deviation estimation layer (layer2), frequency spread estimation layer (layer3), and the learnable convolutional kernels (LCN). We list the error statistics of our PCNet and the networks whose layer1, layer2, layer3, and LCN are respectively frozen in Table VIII. It is observed that our proposed PCNet having all the proposed trainable structures maintains the best registration performance. Specifically, the networks with the modified phase deviation estimation layer (layer2) or learnable convolutional kernels (LCN) frozen are of evident performance degradation, which means the corresponding layers contribute a lot to the registration accuracy.

TABLE VIII

ERROR STATISTICS OF THE FULL PCNET, THE TRAINED NETWORK WHOSE LAYER1, LAYER2, LAYER3, AND LCN ARE RESPECTIVELY FROZEN. THE BEST ONES ARE IN BOLD.

	Mean	Med.	Tri.	Best 25%	Best 50%	Best 75%	Best 95%
Full	6.09	0.20	0.26	0.04	0.08	0.17	3.77
Freezing layer1	6.65	0.20	0.26	0.04	0.09	0.17	4.13
Freezing layer2	7.29	0.22	0.47	0.04	0.09	0.20	5.02
Freezing layer3	6.19	0.22	0.29	0.05	0.10	0.18	3.61
Freezing LCN	8.52	0.23	3.82	0.04	0.09	0.31	6.26

VI. CONCLUSIONS

In this paper we have proposed a network called PCNet for the structure similarity enhancement purpose of image registration task. The prior knowledge of our PCNet are based on the phase congruency theory. PCNet is concise and easy to train thanks to the prior information. The PCNet produces satisfactory registration results on a variety of multispectral

and multimodal datasets though only trained on a small amount of multispectral band images. PCNet performs better than other state-of-the-art similarity enhancement algorithms and feature-based registration algorithms.

A limitation of this work is that the current phase congruency features produced by PCNet is only implemented for the global affine registration, and is unable to cope with the scenes having large parallax or moving objects. For the future work, we will aim at extending our proposed PCNet together with the registration algorithm to nonrigid registration problems.

REFERENCES

- [1] M. Brown and S. Süsstrunk, “Multi-spectral SIFT for scene category recognition,” in *Proceedings of the IEEE Conference on Computer Vision and Pattern Recognition*, 2011, pp. 177–184.
- [2] S. He and R. W. Lau, “Saliency detection with flash and no-flash image pairs,” in *Proceedings of the European Conference on Computer Vision*. Springer, 2014, pp. 110–124.
- [3] G. Petschnigg, R. Szeliski, M. Agrawala, M. Cohen, H. Hoppe, and K. Toyama, “Digital photography with flash and no-flash image pairs,” *ACM Transactions on Graphics*, vol. 23, no. 3, pp. 664–672, 2004.
- [4] V. Balntas, K. Lenc, A. Vedaldi, and K. Mikolajczyk, “Hpatches: A benchmark and evaluation of handcrafted and learned local descriptors,” in *Proceedings of the IEEE Conference on Computer Vision and Pattern Recognition*, 2017, pp. 5173–5182.
- [5] Y. Tarabalka, J. Chanussot, and J. A. Benediktsson, “Segmentation and classification of hyperspectral images using watershed transformation,” *Pattern Recognition*, vol. 43, no. 7, pp. 2367–2379, 2010.
- [6] X. Shen, L. Xu, Q. Zhang, and J. Jia, “Multi-modal and multi-spectral registration for natural images,” in *Proceedings of the European Conference on Computer Vision*. Springer, 2014, pp. 309–324.
- [7] S.-J. Chen, H.-L. Shen, C. Li, and J. H. Xin, “Normalized total gradient: A new measure for multispectral image registration,” *IEEE Transactions on Image Processing*, vol. 27, no. 3, pp. 1297–1310, 2017.
- [8] F. Yasuma, T. Mitsunaga, D. Iso, and S. K. Nayar, “Generalized assorted pixel camera: Postcapture control of resolution, dynamic range, and spectrum,” *IEEE Transactions on Image Processing*, vol. 19, no. 9, pp. 2241–2253, 2010.
- [9] S. Ryu, S. Kim, and K. Sohn, “LAT: Local area transform for cross modal correspondence matching,” *Pattern Recognition*, vol. 63, pp. 218–228, 2017.
- [10] B. Zitova and J. Flusser, “Image registration methods: A survey,” *Image and Vision Computing*, vol. 21, no. 11, pp. 977–1000, 2003.
- [11] D. Firmenichy, M. Brown, and S. Süsstrunk, “Multispectral interest points for RGB-NIR image registration,” in *2011 IEEE International Conference on Image Processing*, 2011, pp. 181–184.
- [12] C. A. Aguilera, A. D. Sappa, and R. Toledo, “LGHHD: A feature descriptor for matching across non-linear intensity variations,” in *2015 IEEE International Conference on Image Processing*, 2015, pp. 178–181.
- [13] J. Li, Q. Hu, and M. Ai, “RIFT: Multi-modal image matching based on radiation-variation insensitive feature transform,” *IEEE Transactions on Image Processing*, vol. 29, pp. 3296–3310, 2019.
- [14] F. Maes, A. Collignon, D. Vandermeulen, G. Marchal, and P. Suetens, “Multimodality image registration by maximization of mutual information,” *IEEE Transactions on Medical Imaging*, vol. 16, no. 2, pp. 187–198, 1997.
- [15] Y. Hel-Or, H. Hel-Or, and E. David, “Matching by tone mapping: Photometric invariant template matching,” *IEEE Transactions on Pattern Analysis and Machine Intelligence*, vol. 36, no. 2, pp. 317–330, 2014.
- [16] S.-Y. Cao, H.-L. Shen, S.-J. Chen, and C. Li, “Boosting structure consistency for multispectral and multimodal image registration,” *IEEE Transactions on Image Processing*, vol. 29, pp. 5147–5162, 2020.
- [17] P. Kovesi, “Phase congruency: A low-level image invariant,” *Psychological Research*, vol. 64, no. 2, pp. 136–148, 2000.
- [18] R. Szeliski *et al.*, “Image alignment and stitching: A tutorial,” *Foundations and Trends® in Computer Graphics and Vision*, vol. 2, no. 1, pp. 1–104, 2007.
- [19] G. P. Penney, J. Weese, J. A. Little, P. Desmedt, D. L. Hill *et al.*, “A comparison of similarity measures for use in 2-D-3-D medical image registration,” *IEEE Transactions on Medical Imaging*, vol. 17, no. 4, pp. 586–595, 1998.
- [20] J. Ma, X. Jiang, A. Fan, J. Jiang, and J. Yan, “Image matching from handcrafted to deep features: A survey,” *International Journal of Computer Vision*, pp. 1–57, 2020.
- [21] D. J. MacKay and D. J. Mac Kay, *Information Theory, Inference and Learning Algorithms*. Cambridge University Press, 2003.
- [22] R. Zabih and J. Woodfill, “Non-parametric local transforms for computing visual correspondence,” in *Proceedings of the European Conference on Computer Vision*. Springer, 1994, pp. 151–158.
- [23] S. Kim, D. Min, B. Ham, M. N. Do, and K. Sohn, “DASC: Robust dense descriptor for multi-modal and multi-spectral correspondence estimation,” *IEEE Transactions on Pattern Analysis and Machine Intelligence*, vol. 39, no. 9, pp. 1712–1729, 2016.
- [24] Y. Tian, X. Yu, B. Fan, F. Wu, H. Heijnen, and V. Balntas, “SOSNet: Second order similarity regularization for local descriptor learning,” in *Proceedings of IEEE Conference on Computer Vision and Pattern Recognition*, 2019, pp. 11016–11025.
- [25] D. DeTone, T. Malisiewicz, and A. Rabinovich, “SuperPoint: Self-supervised interest point detection and description,” in *IEEE Computer Society Conference on Computer Vision and Pattern Recognition Workshops*, 2018, pp. 224–236.
- [26] Z. Luo, L. Zhou, X. Bai, H. Chen, J. Zhang, Y. Yao, S. Li, T. Fang, and L. Quan, “ASLFeat: Learning local features of accurate shape and localization,” in *Proceedings of IEEE Conference on Computer Vision and Pattern Recognition*, 2020, pp. 6589–6598.
- [27] B. Cyganek, *Object detection and recognition in digital images: Theory and practice*. John Wiley & Sons, 2013.
- [28] A. Papoulis and S. U. Pillai, *Probability, random variables, and stochastic processes*. Tata McGraw-Hill Education, 2002.
- [29] R. Reams, “Hadamard inverses, square roots and products of almost semidefinite matrices,” *Linear Algebra and its Applications*, vol. 288, pp. 35–43, 1999.
- [30] V. Nair and G. E. Hinton, “Rectified linear units improve restricted boltzmann machines,” in *Proceedings of the 27th International Conference on International Conference on Machine Learning*, ser. ICML’10. Madison, WI, USA: Omnipress, 2010, p. 807–814.
- [31] J. Han and C. Moraga, “The influence of the sigmoid function parameters on the speed of backpropagation learning,” in *International Workshop on Artificial Neural Networks*. Springer, 1995, pp. 195–201.
- [32] D. Gabor, “Theory of communication. part 1: The analysis of information,” *Journal of the Institution of Electrical Engineers-Part III: Radio and Communication Engineering*, vol. 93, no. 26, pp. 429–441, 1946.
- [33] S. Marčelja, “Mathematical description of the responses of simple cortical cells,” *JOSA*, vol. 70, no. 11, pp. 1297–1300, 1980.
- [34] J. Yosinski, J. Clune, Y. Bengio, and H. Lipson, “How transferable are features in deep neural networks?” in *Advances in Neural Information Processing Systems*, 2014, pp. 3320–3328.
- [35] S. Luan, C. Chen, B. Zhang, J. Han, and J. Liu, “Gabor convolutional networks,” *IEEE Transactions on Image Processing*, vol. 27, no. 9, pp. 4357–4366, 2018.
- [36] B. Zhang, Y. Gao, S. Zhao, and J. Liu, “Local derivative pattern versus local binary pattern: Face recognition with high-order local pattern descriptor,” *IEEE Transactions on Image Processing*, vol. 19, no. 2, pp. 533–544, 2009.
- [37] L. Bottou and O. Bousquet, “The tradeoffs of large scale learning,” in *Advances in Neural Information Processing Systems*, 2008, pp. 161–168.
- [38] S. Abbasi and F. Mokhtarian, “Shape similarity retrieval under affine transform: Application to multi-view object representation and recognition,” in *Proceedings of the IEEE International Conference on Computer Vision*, vol. 1, 1999, pp. 450–455.
- [39] J. Klein and T. Aach, “Multispectral filter wheel cameras: Modeling aberrations for filters in front of lens,” in *Digital Photography VIII*, vol. 8299. International Society for Optics and Photonics, 2012, p. 82990R.
- [40] D. Rueckert, L. I. Sonoda, C. Hayes, D. L. Hill, M. O. Leach, and D. J. Hawkes, “Nonrigid registration using free-form deformations: Application to breast MR images,” *IEEE Transactions on Medical Imaging*, vol. 18, no. 8, pp. 712–721, 1999.
- [41] A. Chakrabarti and T. Zickler, “Statistics of real-world hyperspectral images,” in *Proceedings of the IEEE Conference on Computer Vision and Pattern Recognition*, 2011, pp. 193–200.
- [42] C. Liu, J. Yuen, A. Torralba, J. Sivic, and W. T. Freeman, “Sift flow: Dense correspondence across different scenes,” in *Proceedings of the European Conference on Computer Vision*. Springer, 2008, pp. 28–42.
- [43] M. A. Fischler and R. C. Bolles, “Random sample consensus: A paradigm for model fitting with applications to image analysis and automated cartography,” *Communications of the ACM*, vol. 24, no. 6, pp. 381–395, 1981.